



Moiré flat Chern bands and correlated quantum anomalous Hall states generated by spin-orbit couplings in twisted homobilayer MoS₂

Benjamin T. Zhou ^{*}, Shannon Egan, and Marcel Franz [†]

Department of Physics and Astronomy & Stewart Blusson Quantum Matter Institute, University of British Columbia, Vancouver BC, Canada V6T 1Z4

 (Received 2 July 2021; revised 28 February 2022; accepted 2 March 2022; published 16 March 2022)

We predict that in a twisted homobilayer of transition-metal dichalcogenide MoS₂, spin-orbit coupling in the conduction band states from $\pm K$ valleys, can give rise to moiré flat bands with nonzero Chern numbers in each valley. The nontrivial band topology originates from a unique combination of angular twist and local mirror symmetry breaking in each individual layer, which results in unusual skyrmionic spin textures in momentum space with skyrmion number $\mathcal{S} = \pm 2$. Our Hartree-Fock analysis further suggests that density-density interactions generically drive the system at 1/2-filling into a valley-polarized state, which realizes a correlated quantum anomalous Hall state with Chern number $\mathcal{C} = \pm 2$. Effects of displacement fields are discussed with comparison to nontrivial topology from layer-pseudospin magnetic fields.

DOI: [10.1103/PhysRevResearch.4.L012032](https://doi.org/10.1103/PhysRevResearch.4.L012032)

Introduction. The discovery of possible correlated insulating states [1] and superconductivity [2] in magic-angle twisted bilayer graphene has paved a new avenue toward engineering electronic structures where interactions play a decisive role [3–19]. Lately, nontrivial topological properties brought about by the moiré patterns were also unveiled [20,21]. Under appropriate symmetry breaking conditions, flat bands in twisted graphene acquire nonzero Chern numbers [22–25], which manifest experimentally as quantum anomalous Hall (QAH) states when spin or valley degeneracies are lifted spontaneously through electronic correlations [26–28]. The interplay between correlation and topology uncovered in these systems indicates possibilities for novel topological phases beyond conventional noninteracting theories.

Motivated by advances in twisted graphene systems, explorations into moiré superlattices formed by other two-dimensional materials, such as transition-metal dichalcogenides (TMDs) [29–35] and copper oxides [36,37], have also seen rapid progress recently. In particular, moiré flat bands in a twisted homobilayer TMD formed by the valence band (VB) states in each K valley were shown to carry nonzero Chern numbers [29]. The nontrivial band topology arises from combined effects of moiré potential and interlayer coupling, which act together as a layer-pseudospin magnetic field and create skyrmionic pseudospin textures in superlattice cells. The strong spin-valley locking due to giant Ising-type

spin-orbit coupling (SOC) of order ~ 100 meV [38,39] further entails a possible quantum spin Hall state.

While flat bands from VB states have enjoyed wide interest, moiré physics arising from conduction band (CB) states in twisted TMDs remains largely unexplored. One possible complication lies in the relatively weak SOC in the conduction bands on the scale of a few to tens of meV [39,40], which may cause crossings between spin-up and spin-down moiré bands. Recent works on untwisted TMDs, on the other hand, revealed that the small spin-orbit splitting in CB states, when combined with Rashba SOC introduced by mirror symmetry breaking, can lead to nontrivial Berry phase effects [41–43]. Notably, upon assembling two identical TMD layers into a twisted bilayer, the mirror symmetry is broken locally in each layer [Figs. 1(a) and 1(b)] and Rashba SOC is expected to arise. How this SOC would affect the band topology of twisted TMDs is an outstanding question.

In this Letter we establish a novel topological phase generated by SOC in CB moiré bands in twisted TMDs, which is essentially different from those in twisted graphene [20–25] where SOC is negligible, and those in the VB moiré bands of twisted TMDs where SOC plays no essential role in creating nonzero Chern numbers [29]. Focusing on the specific case of a twisted homobilayer MoS₂ we predict that an interplay among angular twist, local symmetry breaking, and spin-orbit coupling in the CB states creates moiré flat bands with nonzero Chern numbers $\mathcal{C} = \pm 2$, and density-density interactions generically drive the system at 1/2-filling into a valley-polarized correlated QAH state. We further show that the Chern bands generated by SOC stay robust against displacement fields which would otherwise destroy the nontrivial topology from layer pseudospins [29].

Continuum model for twisted homobilayer MoS₂. Stacking two monolayers of MoS₂ with a small relative twist angle θ_0 results in a moiré superlattice with lattice constant $a_M = a/\theta_0$, where a is the lattice constant of each monolayer. The

^{*}Corresponding author: benjamin.zhou@ubc.ca

[†]Corresponding author: franz@phas.ubc.ca

Published by the American Physical Society under the terms of the [Creative Commons Attribution 4.0 International](https://creativecommons.org/licenses/by/4.0/) license. Further distribution of this work must maintain attribution to the author(s) and the published article's title, journal citation, and DOI.

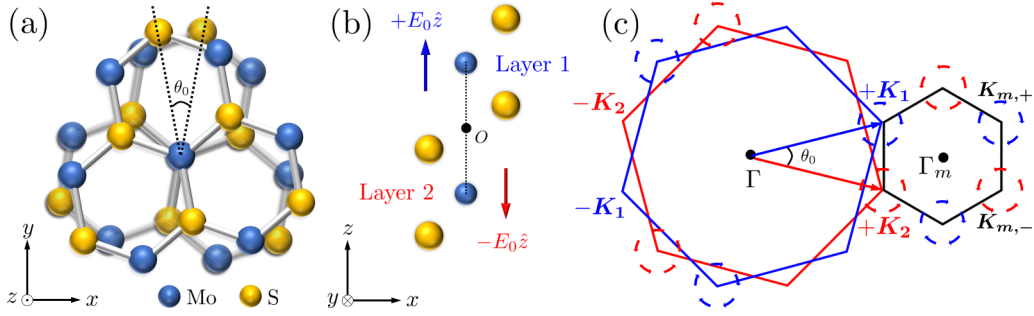


FIG. 1. Schematic crystal structure of twisted bilayer MoS₂ with (a) top view and (b) side view. Electrons in different layers experience opposite effective electric fields due to local lack of mirror symmetry. (c) Moiré Brillouin zone (MBZ) formed by twisting hexagonal Brillouin zones of each layer. The in-plane spinor field exhibits opposite vorticities at $K_{m,+}$ and $K_{m,-}$ of MBZ due to layer-dependent Rashba effects.

system has a symmetry group of $D_3 \otimes \{U_v(1), \mathcal{T}\}$, where $U_v(1)$ stands for valley conservation, \mathcal{T} is for time-reversal symmetry, and the point group D_3 is generated by the three-fold rotation about the z axis (C_{3z}) and a twofold rotation about the y axis (C_{2y}) [Fig. 1(a)]. For an aligned bilayer at $\theta_0 = 0$, the mirror symmetry \mathcal{M}_z about the horizontal 2D mirror plane, which is respected in a monolayer, is broken locally on each layer. This generates uniform electric fields of opposite signs in different layers, which remain effective upon a small angular twist with $\theta_0 \sim 1^\circ$ [Fig. 1(b)]. Based on models of monolayer MoS₂ with broken \mathcal{M}_z [41–43], the effective Hamiltonian for CB minima at $\pm K$ valleys of two twisted isolated layers can be written as

$$\begin{aligned} \mathcal{H}_{0,l}^\xi &= \sum_{k,\alpha\beta} c_{k,l,\alpha}^\dagger h_{l,\alpha\beta}^\xi(\mathbf{k}) c_{k,l,\beta}, \\ h_l^\xi(\mathbf{k}) &= \frac{\hbar^2(\mathbf{k} - \xi \mathbf{K}_l)^2}{2m^*} - \mu + \xi \beta_{so} \sigma_z \\ &\quad + (-1)^l \alpha_{so} [(\mathbf{k} - \xi \mathbf{K}_l) \times \boldsymbol{\sigma}] \cdot \hat{z}, \end{aligned} \quad (1)$$

where $\xi = \pm$ denotes the valley index, $l = 1(2)$ labels the top (bottom) layer, and α, β label the spin indices with the σ matrices representing the usual Pauli matrices for spins. $\mathbf{K}_1 \equiv \mathbf{K}_{m,+}$ and $\mathbf{K}_2 \equiv \mathbf{K}_{m,-}$ are the shifted $+\mathbf{K}$ points on layer 1 and layer 2 [Fig. 1(c)] due to the angular twist of θ_0 equivalent to rotating the top (bottom) layer by an angle $\theta_0/2$ ($-\theta_0/2$) about the z axis. In Eq. (1), $m^* \approx 0.5m_e$ is the CB effective mass at K , and μ is the Fermi energy measured from band minima. The α_{so} term and β_{so} term account for the Rashba SOC and the Ising SOC, respectively. The Ising SOC has a valley-dependent sign due to time-reversal symmetry and causes a splitting of $\Delta_{so} = 2|\beta_{so}|$ in the spin-up and spin-down CB states. The Rashba SOC has a layer-dependent sign imposed by C_{2y} which swaps the two layers. Spatial variations of α_{so} are discussed in the Supplemental Material (SM) [44].

Spatial modulations due to the formation of moiré pattern can be captured by introducing coupling terms between states at \mathbf{k} and $\mathbf{k} + \mathbf{G}_{M,j}$ [23,29], where $\mathbf{G}_{M,j} = -\frac{4\pi}{\sqrt{3}a_M} (\cos \frac{(j-1)\pi}{3}, \sin \frac{(j-1)\pi}{3})$ are the reciprocal vectors of the moiré superlattice. The momentum-space moiré potential is given by

$$\mathcal{H}_M = \sum_k \sum_{j=1}^6 \sum_{l=1,2} \sum_{\alpha=\uparrow,\downarrow} c_{k,l,\alpha}^\dagger V_{l,G_{M,j}} c_{k+\mathbf{G}_{M,j},l,\alpha}, \quad (2)$$

where $V_{l,G_{M,j}} = V_M [\cos \psi - i(-1)^j \sin \psi]$ are complex coupling parameters with amplitude V_M and phase ψ .

The effective interlayer tunneling for states at K valleys is modeled following the general recipe of two-center approximation [4,29], which can be written as

$$\mathcal{H}_T^\xi = -w_0 \sum_k c_{k,1}^\dagger (c_{k,2} + c_{k+\xi \mathbf{G}_{M,2,2}} + c_{k+\xi \mathbf{G}_{M,3,2}}) + \text{H.c.}, \quad (3)$$

where w_0 denotes the effective interlayer tunneling amplitude near K , which is extrapolated to be $w_0 \approx 10$ meV using a combined approach of empirical models and Slater-Koster methods (see the Supplemental Material [44] for details). The total noninteracting continuum model thus reads: $\mathcal{H}_0 = \sum_{\xi=\pm} \sum_{l=1,2} \mathcal{H}_{0,l}^\xi + \mathcal{H}_T^\xi + \mathcal{H}_M$ with parameters tabulated in Table I.

Moiré flat Chern bands and skyrmionic spin textures. From general considerations, level spacings among the lowest moiré bands correspond roughly to the quantization energy $\Delta E \sim \hbar^2 \pi^2 / (2m^* a_M^2)$ of an electron confined in a superlattice cell with size $a_M^2 = a^2 / \theta_0^2$. For $\theta_0 \sim 1^\circ - 2^\circ$, $\Delta E \sim 1 - 10$ meV in twisted MoS₂, which is comparable to the spin-orbit splitting $\Delta_{so} \equiv 2|\beta_{so}| = 3$ meV caused by the Ising SOC [39]. If spin is conserved (e.g., in the absence of Rashba SOC), spin-up and spin-down moiré bands are expected to cross in general.

By setting $\alpha_{so} = 0$ in \mathcal{H}_0 , we find that for $\xi = +$, the first spin-down and the second spin-up moiré bands cross each other for $\theta_0 \in (1.25^\circ, 1.5^\circ)$. As a specific example, spin-resolved moiré bands at $\theta_0 = 1.4^\circ$ with $\alpha_{so} = 0$ are shown in Fig. 2(a). With spin conservation in this case, the spin Chern number is well defined, and the spin-up and spin-down bands involved in the level crossing have Chern numbers ($\mathcal{C}_{1,\downarrow} = +1, \mathcal{C}_{2,\uparrow} = -1$) which originate from the layer-pseudospin magnetic fields as in moiré bands from VB states [29]. Upon turning on α_{so} , crossing points are gapped out by the layer-dependent Rashba SOC which mix the spin-up and spin-down

TABLE I. Parameters used in \mathcal{H}_0 for twisted homobilayer MoS₂ with monolayer lattice constant $a = 3.16$ Å.

μ	α_{so}	β_{so}	V_M	ψ	w_0
0 meV	80 meV Å	-1.5 meV	10 meV	-89.6°	10 meV

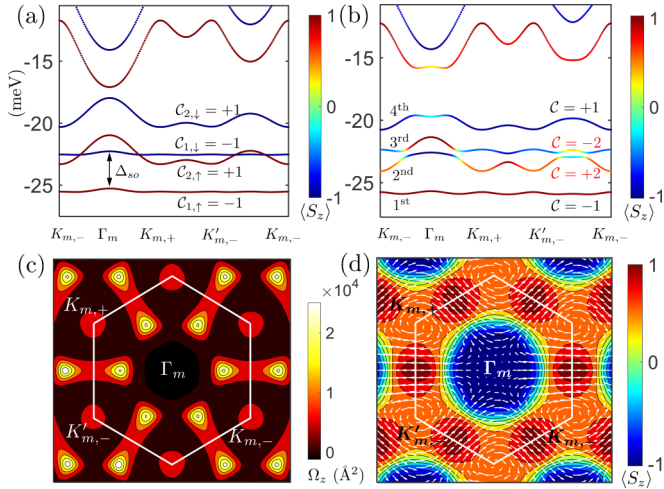


FIG. 2. Moiré bands of valley $\xi = +$ formed by CB states of twisted homobilayer MoS₂ at $\theta_0 = 1.4^\circ$ with (a) $\alpha_{so} = 0$ and (b) $\alpha_{so} \neq 0$. The color bars indicate the out-of-plane spin expectation value $\langle S_z \rangle$ in units of $\hbar/2$. (c) Momentum-space profile of Berry curvature Ω_z in units of \AA^2 in the second moiré band in (b). Large Ω_z of order 10^4\AA^2 emerges as a result of the nontrivial gap induced by SOC. (d) Momentum-space spin texture of the second moiré band in (b). White arrows indicate the in-plane spinor field, which has opposite vorticities at $K_{m,+}$ and $K_{m,-}$ and leads to a nontrivial skyrmion number $\mathcal{S} = +2$. Parameters used are presented in Table I.

species [Fig. 2(b)]. As a result of this mixing, the original $C_{1,\downarrow}$ and $C_{2,\uparrow}$ from layer pseudospins annihilate each other; meanwhile, a new pair of flat bands [second and third bands in Fig. 2(b)] with Chern numbers $\mathcal{C} = \pm 2$ emerge (see SM [44] for details on Chern number calculations). The nontrivial gap induced by Rashba SOC is further signified by giant Berry curvatures of order 10^4\AA^2 in the MBZ [Fig. 2(c)].

The unusual Chern numbers $\mathcal{C} = \pm 2$ arise from a *unique* combination of angular twist and local mirror-symmetry breaking: as moiré bands at opposite $K_{m,+}$ and $K_{m,-}$ points originate from states in different layers [Fig. 1(c)], the layer-dependent Rashba SOC [Eq. (1)] create an in-plane spinor field with opposite vorticities at $K_{m,+}$ and $K_{m,-}$ in the MBZ. This unusual pattern causes the in-plane spin to wind twice as one goes around a loop enclosing the Γ_m point in the MBZ [Fig. 2(d)]. As we confirm numerically, the spin textures of the second and third moiré bands are characterized by nonzero skyrmion numbers $\mathcal{S} = \int d^2k \hat{n}_k \cdot (\partial_k \hat{n}_k \times \partial_{k'} \hat{n}_k) / 4\pi = \pm 2$ (\hat{n}_k : spin orientation of state at \mathbf{k}), and these two bands describe a two-level system with one-to-one correspondence between Chern numbers \mathcal{C} and skyrmion number \mathcal{S} [45].

Correlated QAH state at 1/2-filling. Given the narrow bandwidth $W \approx 1$ meV of moiré Chern bands [Fig. 2(b)], the characteristic Coulomb energy scale $g_C \simeq e^2/\epsilon a_M \approx 10$ meV overwhelms the kinetic energy and correlation physics is expected to arise (assuming $\theta_0 = 1.4^\circ$ and dielectric constant $\epsilon = 10$ [35]). Motivated by the observation that twisted graphene at 3/4-filling can behave as an SU(4)-quantum Hall ferromagnet [23,26–28], and the fact that all CB moiré bands in Fig. 2(b) involves only a twofold valley degeneracy [note that spin SU(2) symmetry is already broken by SOC], we examine correlation effects when the second moiré band is

half-filled. For simplicity we drop the band index n in the following.

Including density-density interactions, the low-energy effective Hamiltonian: $\mathcal{H}_{\text{eff}} = \mathcal{H}_{0,\text{eff}} + \mathcal{H}_{I,\text{eff}}$, where $\mathcal{H}_{0,\text{eff}} = \sum_{\mathbf{k}, \xi = \pm} E_\xi(\mathbf{k}) c_\xi^\dagger(\mathbf{k}) c_\xi(\mathbf{k})$ is the noninteracting part with band energies $E_\xi(\mathbf{k})$, and the interacting Hamiltonian compatible with $U_v(1)$ and \mathcal{T} reads

$$\mathcal{H}_{I,\text{eff}} = \sum_{\mathbf{k}\mathbf{k}'\mathbf{q}, \xi\xi'} \frac{V(\mathbf{q})}{A} \Lambda^\xi(\mathbf{k} + \mathbf{q}, \mathbf{k}) \Lambda^{\xi'}(\mathbf{k}' - \mathbf{q}, \mathbf{k}') \times c_\xi^\dagger(\mathbf{k} + \mathbf{q}) c_\xi^\dagger(\mathbf{k}') c_{\xi'}(\mathbf{k}') c_{\xi'}(\mathbf{k}), \quad (4)$$

where $V(\mathbf{q})$ is the Fourier transform of the two-body interaction, A is the total area of the system, and $\Lambda^\xi(\mathbf{k} + \mathbf{q}, \mathbf{k}) \equiv \langle u_{\xi, \mathbf{k} + \mathbf{q}} | u_{\xi, \mathbf{k}} \rangle$ ($|u_{\xi, \mathbf{k}}\rangle$: periodic part of the Bloch states) are the form factors arising from projecting the density-density interaction to active bands. The general trial Hartree-Fock ground state at 1/2-filling has the form: $|\Phi\rangle = \prod_{\mathbf{k} \in \text{MBZ}} [w_+(\mathbf{k}) c_+^\dagger(\mathbf{k}) + w_-(\mathbf{k}) c_-^\dagger(\mathbf{k})] |\Phi_0\rangle$, where $|\Phi_0\rangle$ is the vacuum state with all lower-lying bands filled, and $w_\xi(\mathbf{k})$ are the variational parameters.

Minimizing $E^\Phi \equiv \langle \Phi | \mathcal{H}_{\text{eff}} | \Phi \rangle$ with mean-field approximations for Fock exchange terms (see SM [44]) leads to a set of self-consistent equations:

$$\begin{aligned} \Delta_+ + \Delta_- &= J_0, \\ \Delta_+ - \Delta_- &= \frac{J_0}{2N} \sum_{\mathbf{k}} \frac{(\Delta_+ - \Delta_-) - \delta(\mathbf{k})}{D(\mathbf{k})}, \\ \Delta_{+-} &= \frac{J_1}{2N} \sum_{\mathbf{k}} \frac{\Delta_{+-}}{D(\mathbf{k})}. \end{aligned} \quad (5)$$

Here J_0 and J_1 denote the mean-field *intravalley* and *intervalley* exchange coupling constants, $\Delta_\xi = J_0 \bar{n}_\xi$ (\bar{n}_ξ : mean occupancy for valley ξ), and Δ_{+-} are the intravalley and intervalley order parameters, which characterize the average energy gains from intravalley and intervalley exchange interactions, respectively. $\delta(\mathbf{k}) \equiv E_+(\mathbf{k}) - E_-(\mathbf{k})$ denotes energy difference between bands from two valleys $\xi = \pm$, $D(\mathbf{k}) = \sqrt{\Delta_{+-}^2 + [\delta(\mathbf{k}) - \Delta_M]^2/4}$, where we introduce the *valley magnetic order* $\Delta_M \equiv \Delta_+ - \Delta_- = J_0(\bar{n}_+ - \bar{n}_-)$.

Solutions of Eq. (5) are divided into two classes: (i) the valley-polarized (VP) state [6,23], in which one out of the two nearly degenerate moiré bands from two valleys is fully filled, with spontaneous \mathcal{T} -symmetry breaking: $\Delta_M = \xi J_0$, $\Delta_{+-} = 0$, $w_\xi(\mathbf{k}) = 1$. (ii) The intervalley coherent (IVC) state, in which the Slater determinant is formed by coherent superpositions of states from the two valleys, with spontaneous $U_v(1)$ -symmetry breaking [6,23,24]: $\Delta_M = 0$, $\Delta_{+-} \approx J_1/2$, $w_{+,-}(\mathbf{k}) \neq 0$. By comparing the energies of the VP and IVC states, we obtain the mean-field J_0 - J_1 phase diagram for the range $0.3g_C \leq J_0, J_1 \leq g_C$ [Fig. 3(a)]. The IVC state is favored throughout the entire $J_1 \geq J_0$ regime, while the VP phase takes up most of the $J_1 < J_0$ regime. By tuning J_0/J_1 across the phase boundary [green dashed line in Fig. 3(a)], a first-order transition occurs at $J_0 \simeq J_1$ [Fig. 3(b)].

It is worth noting that given a general repulsive interaction $V(\mathbf{q}) > 0$, the inequality $2|\Lambda^+(\mathbf{k}', \mathbf{k})| |\Lambda^-(\mathbf{k}, \mathbf{k}')| \leq |\Lambda^+(\mathbf{k}', \mathbf{k})|^2 + |\Lambda^-(\mathbf{k}, \mathbf{k}')|^2$ together with \mathcal{T} symmetry leads to $J_0 \geq J_1$, regardless of details of the form factors and the

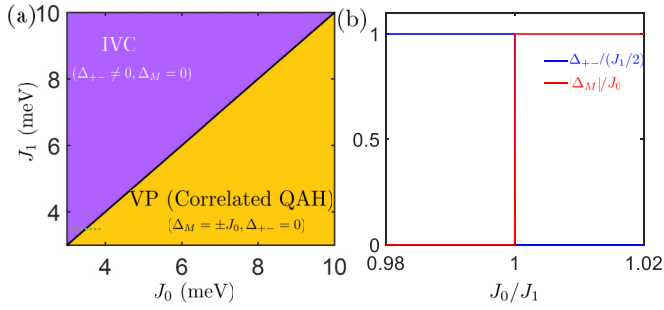


FIG. 3. (a) J_0 - J_1 phase diagram of the system with the second moiré band at 1/2-filling. Under repulsive density-density interactions, only the $J_1 \leq J_0$ regime can be accessed [44], where the valley-polarized (VP) state is generically favored and the system becomes a correlated QAH insulator. (b) Evolutions of the order parameters Δ_{+-} and $\Delta_M \equiv \Delta_+ - \Delta_-$ as the ratio J_0/J_1 is tuned along the line cut [green dashed line in (a)] across the phase boundary. A first-order transition happens at the critical point $J_0 \simeq J_1$.

microscopic interaction [44]. Thus, electron correlations most likely drive the system at 1/2-filling into a \mathcal{T} -broken VP state, which realizes a correlated QAH state with $\mathcal{C} = \pm 2$. The case of general filling away from 1/2 is discussed in SM [44].

Effects of displacement fields and comparison with Chern bands from layer pseudospins. As shown in Fig. 2(a), with $\alpha_{s_0} = 0$, nonzero Chern numbers also arise in CB moiré bands due to layer pseudospin magnetic fields, with the same origin as those in VB moiré bands [29]. Thus, two different mechanisms for moiré Chern bands, one from layer pseudospin and the other from SOCs, *coexist* in the CB moiré bands. In contrast, the Rashba SOC is unimportant in the VB moiré bands where spin-up and spin-down bands are separated by 100–400 meV [39], and the VB moiré band topology is governed by layer pseudospin alone.

The nontrivial topology from layer pseudospin is shown to be prone to displacement fields which can destroy the skyrmionic pseudospin textures by polarizing the layer pseudospins [29]. On the other hand, the SOC mechanism has an independent origin in the avoided level crossings between spin-up and spin-down bands and does not require nontrivial layer pseudospin textures. Thus one would expect the nontrivial band topology in the CB moiré bands to be more robust against displacement fields than its VB counterpart.

To demonstrate the effects of displacement fields, we follow Ref. [29] and introduce a layer-dependent potential $V_{D,l} = (-1)^l V_z/2$ ($l = 1, 2$) in \mathcal{H}_0 . The moiré bands at $\theta_0 = 1.4^\circ$ under finite V_z are shown in Fig. 4(a), where we set $V_z = 4$ meV strong enough to destroy the nontrivial topology generated by layer pseudospins [Fig. 4(b)]. Clearly the avoided level crossings still occur and a pair of Chern bands with Chern numbers $(+1, -1)$ remain. The Chern number is reduced from $\mathcal{C} = \pm 2$ to $\mathcal{C} = \pm 1$ under V_z because the displacement field drives a band inversion near $\mathbf{K}_{m,+}$ and mediates a Chern number exchange $\Delta\mathcal{C} = \pm 1$ between the first and second moiré bands.

The topological phase diagram for CB moiré bands as a function of θ_0 and V_z is shown in Fig. 4(b). Due to the extra mechanism from SOCs, the critical displacement field for the nontrivial topological regime is enhanced to be V_z^{c2} , which is 2–4 times of the critical V_z^{c1} (yellow dashed line) needed

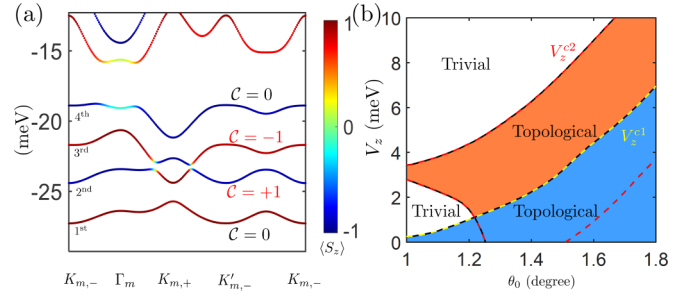


FIG. 4. (a) CB Moiré bands for valley $\xi = +$ of twisted bilayer MoS₂ at $\theta_0 = 1.4^\circ$ and $V_z = 4$ meV. Under finite V_z , spin-up and spin-down bands still cross, and the avoided level crossing due to SOC result in a pair of bands with $\mathcal{C} = \pm 1$. (b) Topological phase diagram of CB moiré bands as a function of θ_0 and V_z , with an upper boundary V_z^{c2} of the entire topological regime. Yellow dashed line: Critical V_z^{c1} above which nontrivial topology generated by layer pseudospin is destroyed. Values of V_z^{c1} are similar to those found in VB moiré bands [29]. Area enclosed by the red dashed lines: Regime with level crossings between spin-up and spin-down CB moiré bands when $\alpha_{s_0} = 0$. Area in orange: Topological regime where layer pseudospin mechanism in Ref. [29] fails.

to destroy the layer pseudospin mechanism for $\theta_0 \sim 1^\circ$ (V_z^{c1} obtained by setting $\alpha_{s_0} = 0$ in \mathcal{H}_0). Importantly, there is a wide parameter regime in the phase diagram (depicted in orange) where the layer pseudospin mechanism proposed in Ref. [29] fails while the CB moiré bands remain topological, which confirms that the CB states are more robust than VB states against displacement fields.

Conclusion and discussions. While on-going activities in twisted TMDs have focused mainly on VB moiré bands [29–35], our proposal of moiré Chern bands generated by SOC opens a new pathway into the largely unknown territory of CB moiré physics. When these Chern bands are half-filled, according to our predictions, electron interactions can lead to a spontaneously \mathcal{T} -broken VP phase and realize a correlated QAH state, which will manifest itself through quantized Hall conductance in transport measurements.

To realize the topological moiré bands generated by SOC, any finite Rashba SOC which is allowed by the D_3 symmetry of the system would be sufficient, in principle, to induce a nontrivial gap. Notably, as MoS₂ is intrinsically semiconducting (with Fermi level ~ 0.8 eV below the conduction band edge) [38,39,46], it is necessary to gate the chemical potential such that the CB moiré bands are filled in the first place. With the dual-gate setup used widely in experiments [1,34], local mirror symmetry breaking can be further enhanced by interfacial contact with gating electrodes, which enhances the SOC gap in the noninteracting bands. Due to the correlated nature of the QAH state at 1/2-filling, the actual topological gap to be manifested experimentally is not solely determined by the SOC gap in the noninteracting bands; instead it should be largely governed by the intravalley exchange coupling $J_0 \sim 10$ meV for $\theta_0 \sim 1^\circ$ [44]. This sizable correlation-induced topological gap will reduce complications of disorder and thermal effects in experimental detection of the predicted correlated QAH state. However, as θ_0 increases, correlation effects become weaker and the moiré bands more dispersive,

thus the predicted correlated QAH phase would be less robust in the large twist angle regime.

B.T.Z. thanks Z. Wu and Z. Ye for inspiring discussions on experimental aspects of twisted MoS₂. This work was sup-

ported by NSERC and the Canada First Research Excellence Fund, Quantum Materials and Future Technologies Program. B.T.Z. further acknowledges the support of the Croucher Foundation.

-
- [1] Y. Cao, V. Fatemi, A. Demir, S. Fang, S. L. Tomarken, J. Y. Luo, J. D. Sanchez-Yamagishi, K. Watanabe, T. Taniguchi, E. Kaxiras, R. C. Ashoori, and P. Jarillo-Herrero, Correlated insulator behaviour at half-filling in magic-angle graphene superlattices, *Nature (London)* **556**, 80 (2018).
- [2] Y. Cao, V. Fatemi, S. Fang, K. Watanabe, T. Taniguchi, E. Kaxiras, and P. Jarillo-Herrero, Unconventional superconductivity in magic-angle graphene superlattices, *Nature (London)* **556**, 43 (2018).
- [3] S. Carr, D. Massatt, S. Fang, P. Cazeaux, M. Luskin, and E. Kaxiras, Twistronics: Manipulating the electronic properties of two-dimensional layered structures through their twist angle, *Phys. Rev. B* **95**, 075420 (2017).
- [4] R. Bistritzer and A. H. MacDonald, Moiré bands in twisted double-layer graphene, *Proc. Natl. Acad. Sci. USA* **108**, 12233 (2011).
- [5] E. Y. Andrei and A. H. MacDonald, Graphene bilayers with a twist, *Nat. Mater.* **19**, 1265 (2020).
- [6] H. C. Po, L. Zou, A. Vishwanath, and T. Senthil, Origin of Mott Insulating Behavior and Superconductivity in Twisted Bilayer Graphene, *Phys. Rev. X* **8**, 031089 (2018).
- [7] N. F. Q. Yuan and L. Fu, Model for the metal-insulator transition in graphene superlattices and beyond, *Phys. Rev. B* **98**, 045103 (2018).
- [8] M. Koshino, N. F. Q. Yuan, T. Koretsune, M. Ochi, K. Kuroki, and L. Fu, Maximally Localized Wannier Orbitals and the Extended Hubbard Model for Twisted Bilayer Graphene, *Phys. Rev. X* **8**, 031087 (2018).
- [9] H. Isobe, N. F. Q. Yuan, and L. Fu, Unconventional Superconductivity and Density Waves in Twisted Bilayer Graphene, *Phys. Rev. X* **8**, 041041 (2018).
- [10] J. Kang and O. Vafek, Symmetry, Maximally Localized Wannier States, and a Low-Energy Model for Twisted Bilayer Graphene Narrow Bands, *Phys. Rev. X* **8**, 031088 (2018).
- [11] F. Wu, A. H. MacDonald, and I. Martin, Theory of Phonon-Mediated Superconductivity in Twisted Bilayer Graphene, *Phys. Rev. Lett.* **121**, 257001 (2018).
- [12] C.-C. Liu, L.-D. Zhang, W.-Q. Chen, and F. Yang, Chiral Spin Density Wave and $d + id$ Superconductivity in the Magic-Angle-Twisted Bilayer Graphene, *Phys. Rev. Lett.* **121**, 217001 (2018).
- [13] B. Lian, Z. Wang, and B. A. Bernevig, Twisted Bilayer Graphene: A Phonon-Driven Superconductor, *Phys. Rev. Lett.* **122**, 257002 (2019).
- [14] J. González and T. Stauber, Kohn-Luttinger Superconductivity in Twisted Bilayer Graphene, *Phys. Rev. Lett.* **122**, 026801 (2019).
- [15] M. Xie and A. H. MacDonald, Nature of the Correlated Insulator States in Twisted Bilayer Graphene, *Phys. Rev. Lett.* **124**, 097601 (2020).
- [16] Y. Jiang, X. Lai, K. Watanabe, T. Taniguchi, K. Haule, J. Mao, and E. Y. Andrei, Charge order and broken rotational symmetry in magic-angle twisted bilayer graphene, *Nature (London)* **573**, 91 (2019).
- [17] X. Lu, P. Stepanov, W. Yang, M. Xie, M. A. Aamir, I. Das, C. Urgell, K. Watanabe, T. Taniguchi, G. Zhang, A. Bachtold, A. H. MacDonald, and D. K. Efetov, Superconductors, orbital magnets and correlated states in magic-angle bilayer graphene, *Nature (London)* **574**, 653 (2019).
- [18] Y. Choi, J. Kemmer, Y. Peng, A. Thomson, H. Arora, R. Polshi, Y. Zhang, H. Ren, J. Alicea, G. Refael, F. von Oppen, K. Watanabe, T. Taniguchi, and S. Nadj-Perge, Electronic correlations in twisted bilayer graphene near the magic angle, *Nat. Phys.* **15**, 1174 (2019).
- [19] Y. Xie, B. Lian, B. Jäck, X. Liu, C.-L. Chiu, K. Watanabe, T. Taniguchi, B. A. Bernevig, and A. Yazdani, Spectroscopic signatures of many-body correlations in magic-angle twisted bilayer graphene, *Nature (London)* **572**, 101 (2019).
- [20] J. Liu, J. Liu, and X. Dai, Pseudo Landau level representation of twisted bilayer graphene: Band topology and implications on the correlated insulating phase, *Phys. Rev. B* **99**, 155415 (2019).
- [21] Z. Song, Z. Wang, W. Shi, G. Li, C. Fang, and B. A. Bernevig, All Magic Angles in Twisted Bilayer Graphene are Topological, *Phys. Rev. Lett.* **123**, 036401 (2019).
- [22] N. Bultinck, S. Chatterjee, and M. P. Zaletel, Mechanism for Anomalous Hall Ferromagnetism in Twisted Bilayer Graphene, *Phys. Rev. Lett.* **124**, 166601 (2020).
- [23] Y.-H. Zhang, D. Mao, Y. Cao, P. Jarillo-Herrero, and T. Senthil, Nearly flat Chern bands in moiré superlattices, *Phys. Rev. B* **99**, 075127 (2019).
- [24] Y.-H. Zhang, D. Mao, and T. Senthil, Twisted bilayer graphene aligned with hexagonal boron nitride: Anomalous Hall effect and a lattice model, *Phys. Rev. Research* **1**, 033126 (2019).
- [25] W.-Y. He, D. Goldhaber-Gordon, and K. T. Law, Giant orbital magnetoelectric effect and current-induced magnetization switching in twisted bilayer graphene, *Nat. Commun.* **11**, 1650 (2020).
- [26] A. L. Sharpe, E. J. Fox, A. W. Barnard, J. Finney, K. Watanabe, T. Taniguchi, M. A. Kastner, and D. Goldhaber-Gordon, Emergent ferromagnetism near three-quarters filling in twisted bilayer graphene, *Science* **365**, 605 (2019).
- [27] M. Serlin, C. L. Tschirhart, H. Polshyn, Y. Zhang, J. Zhu, K. Watanabe, T. Taniguchi, L. Balents, and A. F. Young, Intrinsic quantized anomalous Hall effect in a moiré heterostructure, *Science* **367**, 900 (2020).
- [28] K. P. Nuckolls, M. Oh, D. Wong, B. Lian, K. Watanabe, T. Taniguchi, B. A. Bernevig, and A. Yazdani, Strongly correlated Chern insulators in magic-angle twisted bilayer graphene, *Nature (London)* **588**, 610 (2020).
- [29] F. Wu, T. Lovorn, E. Tutuc, I. Martin, and A. H. MacDonald, Topological Insulators in Twisted Transition Metal Dichalcogenide Homobilayers, *Phys. Rev. Lett.* **122**, 086402 (2019).
- [30] F. Wu, T. Lovorn, E. Tutuc, and A. H. MacDonald, Hubbard Model Physics in Transition Metal Dichalco-

- genide Moiré Bands, *Phys. Rev. Lett.* **121**, 026402 (2018).
- [31] Z. Zhang, Y. Wang, K. Watanabe, T. Taniguchi, K. Ueno, E. Tutuc, and B. J. LeRoy, Flat bands in twisted bilayer transition metal dichalcogenides, *Nat. Phys.* **16**, 1093 (2020).
- [32] Y. Tang, L. Li, T. Li, Y. Xu, S. Liu, K. Barmak, K. Watanabe, T. Taniguchi, A. H. MacDonald, J. Shan, and K. F. Mak, Simulation of Hubbard model physics in WSe₂/WS₂ moiré superlattices, *Nature (London)* **579**, 353 (2020).
- [33] E. C. Regan *et al.*, Mott and generalized Wigner crystal states in WSe₂/WS₂ moiré superlattices, *Nature (London)* **579**, 359 (2020).
- [34] L. Wang *et al.*, Correlated electronic phases in twisted bilayer transition metal dichalcogenides, *Nat. Mater.* **19**, 861 (2020).
- [35] Z. Bi and L. Fu, Excitonic density wave and spin-valley superfluid in bilayer transition metal dichalcogenide, *Nat. Commun.* **12**, 642 (2021).
- [36] O. Can, T. Tummuru, R. P. Day, I. Elfimov, A. Damascelli, and M. Franz, High-temperature topological superconductivity in twisted double-layer copper oxides, *Nat. Phys.* **17**, 519 (2021).
- [37] P. A. Volkov, J. H. Wilson, and J. H. Pixley, Magic angles and current-induced topology in twisted nodal superconductors, [arXiv:2012.07860](https://arxiv.org/abs/2012.07860).
- [38] D. Xiao, G.-B. Liu, W. Feng, X. Xu, and W. Yao, Coupled Spin and Valley Physics in Monolayers of MoS₂ and Other Group-VI Dichalcogenides, *Phys. Rev. Lett.* **108**, 196802 (2012).
- [39] G.-B. Liu, W.-Y. Shan, Y. Yao, W. Yao, and D. Xiao, Three-band tight-binding model for monolayers of group-VIB transition metal dichalcogenides, *Phys. Rev. B* **88**, 085433 (2013).
- [40] K. Kořmider, J. W. González, and J. Fernández-Rossier, Large spin splitting in the conduction band of transition metal dichalcogenide monolayers, *Phys. Rev. B* **88**, 245436 (2013).
- [41] B. T. Zhou, K. Taguchi, Y. Kawaguchi, Y. Tanaka, and K. T. Law, Spin-orbit coupling induced valley Hall effects in transition-metal dichalcogenides, *Commun. Phys.* **2**, 26 (2019).
- [42] K. Taguchi, B. T. Zhou, Y. Kawaguchi, Y. Tanaka, and K. T. Law, Valley Edelstein effect in monolayer transition-metal dichalcogenides, *Phys. Rev. B* **98**, 035435 (2018).
- [43] K.-H. Kim and H.-W. Lee, Berry curvature in monolayer MoS₂ with broken mirror symmetry, *Phys. Rev. B* **97**, 235423 (2018).
- [44] See Supplemental Material at <http://link.aps.org/supplemental/10.1103/PhysRevResearch.4.L012032> for details on: (i) calculation of effective interlayer tunneling parameter w_0 ; (ii) method used for computing Chern numbers in the moiré bands; (iii) self-consistent Hartree-Fock calculations for correlated ground at 1/2-filling and discussions on the case of general filling; and (iv) estimate of spatial variation in Rashba SOC strength, which includes Refs. [47–50].
- [45] B. A. Bernevig, *Topological Insulators and Topological Superconductors* (Princeton University Press, Princeton, NJ, 2013), Chap. 8.3.
- [46] K. F. Mak, C. Lee, J. Hone, J. Shan, and T. F. Heinz, Atomically Thin MoS₂: A New Direct-Gap Semiconductor, *Phys. Rev. Lett.* **105**, 136805 (2010).
- [47] K. D. Rasamani, F. Alimohammadi, and Y. Sun, Interlayer-expanded MoS₂, *Mater. Today* **20**, 83 (2017).
- [48] F. Zahid, L. Liu, Y. Zhu, J. Wang, and H. Guo, A generic tight-binding model for monolayer, bilayer and bulk MoS₂, *AIP Adv.* **3**, 052111 (2013).
- [49] T. Fukui, Y. Hatsugai, and H. Suzuki, Chern Numbers in Discretized Brillouin Zone: Efficient Method of Computing (Spin) Hall Conductances, *J. Phys. Soc. Jpn.* **74**, 1674 (2005).
- [50] Q.-F. Yao, J. Cai, W.-Y. Tong, S.-J. Gong, J.-Q. Wang, X. Wan, C.-G. Duan, and J. H. Chu, Manipulation of the large Rashba spin splitting in polar two-dimensional transition-metal dichalcogenides, *Phys. Rev. B* **95**, 165401 (2017).